Anatomy of strike-slip fault tsunami genesis

Ahmed Elbanna[a,b] , Mohamed Abdelmeguid[a] , Xiao Ma[a] , Faisal Amlani[c] , Harsha S. Bhat[d] , Costas Synolakis[e,f],
and Ares J. Rosakis[g,1]

[a]Department of Civil and Environmental Engineering, University of Illinois at Urbana–Champaign, Urbana, IL 61801; [b]Beckman Institute for Advanced Science and Technology, University of Illinois at Urbana–Champaign, Urbana, IL 61801; [c]Department of Aerospace and Mechanical Engineering, University of Southern California, Los Angeles, CA 90089; [d]Laboratoire de Géologie, École Normale Supérieure, CNRS-UMR 8538, PSL Research University, 75006 Paris, France; [e]Department of Civil and Environmental Engineering, University of Southern California, Los Angeles, CA 90089; [f]Research Centre for Atmospheric Physics and Climatology, Academy of Athens, 10680 Athens, Greece; and [g]Graduate Aerospace Laboratories, California Institute of Technology, Pasadena, CA 91125

Tsunami generation from earthquake-induced seafloor deformations has long been recognized as a major hazard to coastal areas. Strike-slip faulting has generally been considered insufficient for triggering large tsunamis, except through the generation of submarine landslides. Herein, we demonstrate that ground motions due to strike-slip earthquakes can contribute to the generation of large tsunamis (>1 m), under rather generic conditions. To this end, we developed a computational framework that integrates models for earthquake rupture dynamics with models of tsunami generation and propagation. The three-dimensional time-dependent vertical and horizontal ground motions from spontaneous dynamic rupture models are used to drive boundary motions in the tsunami model. Our results suggest that supershear ruptures propagating along strike-slip faults, traversing narrow and shallow bays, are prime candidates for tsunami generation. We show that dynamic focusing and the large horizontal displacements, characteristic of strike-slip earthquakes on long faults, are critical drivers for the tsunami hazard. These findings point to intrinsic mechanisms for sizable tsunami generation by strike-slip faulting, which do not require complex seismic sources, landslides, or complicated bathymetry. Furthermore, our model identifies three distinct phases in the tsunamic motion, an instantaneous dynamic phase, a lagging coseismic phase, and a postseismic phase, each of which may affect coastal areas differently. We conclude that near-source tsunami hazards and risk from strike-slip faulting need to be re-evaluated.

tsunamis in bays | strike-slip faults | supershear ruptures | vertical and horizontal bathymetry motions | run-up

Tsunamis are classically defined as long, free-surface water waves generated by impulsive geological events (1). Tsunamis may be triggered by earthquakes, volcanoes, landslides or slumps, submarine gas releases, and meteorite impacts. Over the past century, tsunamis alone have been responsible for the loss of hundreds of thousands of lives and trillions of dollars in damage to the environment and built infrastructure (2, 3). This makes tsunamis among the most destructive natural hazards. Quantitative and predictive modeling of tsunamis is crucial for reducing the impact of these events and for enabling better preparedness plans.

Generally, the tsunami impact is associated with the size of the vertical seafloor motion. Massive tsunamis are generally attributed to great earthquakes along subduction-zone plate boundaries, such as the 2004 M~ 9.2 Sumatran and the 2011 M~ 9.0 Tohoku-Oki events. Strike-slip faults, which generally generate small seafloor vertical displacements, are generally considered unfavorable for tsunami generation (4). Field observations, however, suggest that in many cases (5–9), strike-slip motion can indeed generate tsunami waves, supposedly by triggering landslides (10). Even though a small fraction of all tsunamis studied this far are believed to be triggered by strike-slip motion (11), their possible devastating humanitarian impact warrants further investigation into this particular mechanism for tsunami genesis.

The September 2018 Mw 7.5 Sulawesi earthquake occurred on the Palu-Koro (P-K) strike-slip fault system and caused an unexpected localized tsunami, atypical in its impact for this type of fault motion (12). Bao et al. (13) and Socquet et al. (14) were among the first to recognize the supershear nature of this earthquake (13, 14). Several authors (13, 15–17) have postulated that submarine landslides, triggered by the earthquake's strong ground motion, were the primary source for the devastating tsunami. Ulrich et al. (18) argued that the earthquake displacements were critical to the tsunami generation. Using a three-dimensional (3D) dynamic rupture model that emulated the earthquake propagation on the geometrically complex P-K fault system and coupling it with the two-dimensional (2D) shallow-water wave equations, they demonstrated that the fault slip, which included a nonnegligible rake and dip slip components, may only trigger tsunami waves of the order of a meter. Their conclusions, however, are confounded by the specifics of the complex Palu Bay bathymetry and the complex geometry of the P-K fault system.

Amlani et al. (19) utilized near-fault GPS data to first conclusively demonstrate that the P-K rupture was indeed supershear. They then recovered a crucial term in the shallow-water wave equation by including the time derivative of the seafloor vertical displacements and, thus, ensured correct mass conservation (20). This forcing was implemented in the context of a onedimensional (1D) nonlinear shallow-water wave model and a simple bathymetry, driven dynamically by the vertical components of the motion computed from a 3D dynamic rupture simulation of a supershear earthquake along a strike-slip fault. They showed that explicitly accounting for the dynamic source

Significance

Our work has uncovered unexpected potential for strike-slip faults to generate devastating tsunamis, without necessarily triggering coseismic underwater landslides or slumps with their associated wave generation. This is a previously unrecognized hazard for coastal cities worldwide. The risk is higher for supershear earthquakes, as in the 1999 Izmit and the 2018 Palu events, which may be the case for an earthquake rupturing the northern segment of the San Andreas Fault.

effects uncovers high-frequency details in the early phases of the tsunami motion. They claimed these details may get missed if only the static seafloor displacements are used. However, they did not consider the effect of horizontal displacements in the ground motion on deforming the bathymetry. Furthermore, their 1D model could not account for the dramatic focusing effect introduced by water waves converging at, and subsequently reflected and refracted from, the apex of any narrow bay. These limitations possibly led to a noticeable underprediction of the calculated amplitude of the waves.

The question, therefore, remains whether generic strike-slip faults, in the absence of secondary sources, such as coseismic underwater landslides, can generate large tsunamis. This question has important ramifications, as several metropolitan areas worldwide are located near bays (6, 7, 21–23) that are traversed by strike-slip faults similar to the P-K system. Furthermore, while early warning for far-field tsunamis (1, 24, 25) based on hydrodynamic inversions is now fairly routine, at least in the North Pacific, little or no early warning is possible for near-field tsunamis, in which the tsunami originates just a few kilometers away from the coastline. Most field scientists agree that, thus far, for coastal residents, earthquake shaking is the warning for an impending tsunami from a nearshore source (26, 27).

To shed light on the basic mechanisms through which strike-slip faults may cause damaging tsunamis, we have developed a computational framework that integrates mechanistic models for earthquake rupture dynamics with hydrodynamic models for tsunami generation and propagation. Possibly with a few exceptions, the initial condition in tsunami models is computed by using the static algorithms of Mansinha and Smylie (28), subsequently parameterized by Okada (29), which translate finite fault slip models into static seafloor displacements. In recent years, there has been an increased interest in developing models that account for dynamic generation (18, 30–33). Here, we use our dynamic generation model and focus on a planar strike-slip fault traversing a shallow bay with a simple geometry. Tsunami evolution over a more complex bathymetry may hide the effects of the dynamic rupture. Our approach is thus designed to unravel the underlying physics governing tsunami generation due to the intrinsic nature of strike-slip faulting. In other words, we seek to understand the basic phenomenology first, before applying our model to complex geophysical geometries.

The 2018 Palu earthquake and tsunami highlighted the complex dynamics of tsunamis generated by intersonic earthquakes. In supershear, or intersonic, earthquakes (34–40), the rupture tip propagates faster than the shear wave speed (41–43). This leads to the emergence of large localized deformation bands along the shear shock wave fronts, also known as Mach cones (34, 35, 38, 39, 44). Dunham and Bhat (38) proved the presence of a second Mach front associated with Rayleigh waves that carry significant vertical motion, moderately attenuated, to large distances. When such earthquakes occur within a narrow bay, the associated large horizontal displacements, as well as the moderately attenuated vertical displacements (34, 39, 45), along the shear and Rayleigh shock wave fronts may cause significant motion in the bay boundaries, which, just as with a paddle wavemaker, could lead to the displacement of large volumes of water. Furthermore, in these scenarios, the triggered tsunami may exhibit multiple characteristic time scales, ranging from a few seconds to several minutes.

In the following sections, we investigate the synergistic interactions between rupture speed, seafloor ground motions, and bay geometry. We also examine several distinct features of the tsunami, including the emergence of an instantaneous dynamic phase and a slower coseismic phase, both of which lead to a gravity-driven postseismic phase.

Coupled Earthquake–Tsunami Framework

Earthquake Model. We model a bilaterally expanding earthquake rupture by solving the elastodynamic wave equation, for the bulk displacement field $u_i(\mathbf{x}, t)$ for $i = 1, 2, 3$, in a 3D linear elastic medium surrounding a vertically dipping rectangular planar fault. The Cartesian coordinate system is given by $\mathbf{x} = x_i e_i$, where e_i are the fixed mutually orthogonal unit vectors. We prescribe absorbing boundary conditions along the lateral and bottom boundaries of the domain to minimize artificial wave reflection due to simulation domain truncation. The top boundary, which corresponds to the seafloor, is modeled as a free surface. We impose an initially uniform shear stress everywhere on the fault surface, except for a small, squared, localized region that we overstress to forcefully nucleate the rupture. The initial shear stress is applied along the fault strike-parallel direction with zero component in the dip direction. Furthermore, a uniform compressive stress acts on the fault.

The fault strength is governed by a linear slip-weakening frictional law. Fault slip starts at a point when the shear stress reaches the static shear strength level, given by the product of the static friction coefficient and the compressive normal stress. The stress then decreases linearly with increasing slip, over a characteristic slip-weakening distance, to the dynamic shear strength, set by the product of the constant dynamic friction coefficient and the compressive stress.

The terminal speed of the nucleated rupture depends on the fault stress level, as measured by the strength parameter S^*, which is given by the ratio of two stress measures (42, 46, 47). The first is the difference between static shear strength and initial shear stress. The second is the difference between initial shear stress and dynamic shear strength. The S^* parameter thus quantifies the proximity of the fault initial stress state to its static strength, scaled relative to its dynamic stress drop. High S^* values, corresponding to low-stressed faults, generally favor sub-Rayleigh ruptures with the rupture propagation speed limited by the Rayleigh wave speed. Low values of S^*, corresponding to highly stressed faults, enable the rupture tip to break the shear wave speed barrier and become supershear, propagating at intersonic speeds.

In this work, we vary the value of the initial shear stress to simulate both supershear and sub-Rayleigh ruptures. We note that varying the initial shear stress will change the stress drop and slip accumulation during the two rupture scenarios. This, in turn, will affect some of the tsunami-generation features. More details of the earthquake model are given in *Materials and Methods*.

Tsunami Model. We model the tsunami initiation and subsequent propagation in the bay using the 2D nonlinear shallow-water equations, assuming an inviscid and incompressible flow model (30, 48). The coupling between the earthquake and tsunami models is realized through the time-dependent 3D seafloor displacement and velocity fields computed from the dynamic rupture simulation and then imported to the tsunami model as time-dependent boundary motions. Specifically, we solve the following set of nonlinear equations (49):

$$h^*_{,t} + (\hat{v}_\beta h^*)_{,\beta} = 0 \qquad \beta = 1, 2, \qquad \textbf{[1a]}$$

$$\hat{v}_{\alpha,t} + \hat{v}_\beta(\hat{v}_{\alpha,\beta}) + gh^*_{,\alpha} = gH_{,\alpha} \qquad \alpha, \beta = 1, 2. \qquad \textbf{[1b]}$$

Here, t is time, $H = H(x_1, x_2, t)$ is the depth of the bay, and $\hat{v}_\alpha = \hat{v}_\alpha(x_1, x_2, t)$ are the depth-averaged in-plane water particle velocities for $\alpha = 1, 2$. $(.)_{,\alpha}$ denotes the differentiation of the relevant variable with respect to the coordinate x_α, and g is the gravitational acceleration. We define $h^* = h + H$, where h is the vertical sea-surface displacement measured from the initially undisturbed sea-surface level ($x_3 = 0$), and h^* is the total water

column height. We note that in Eq. **1a**, $h_{,t}^* = h_{,t} + H_{,t}$. Thus, by accounting explicitly for the $H_{,t}$ term, we are using both the time-dependent seafloor displacements and the seafloor particle velocities in the dynamic model, and not just the time-dependent displacements.

For a general bathymetry, horizontal motions could contribute to the water-surface motion, as recognized by Tanioka and Satake (50). For a seafloor displacement $u_i^s \equiv u_i(\mathbf{x}, t) \; \forall \; \mathbf{x} \in \Gamma_s$, where Γ_s is the free surface in the earthquake model, and for an initial static bathymetry profile $H_o(x_1, x_2) = H(x_1, x_2, 0)$, the seafloor motion is computed as follows (51):

$$H(x_1, x_2, t) = H_o(x_1 - u_1^s, x_2 - u_2^s) - u_3^s. \qquad \text{[2]}$$

The expression in Eq. **2** is general enough to account for any slope and is not restricted by the smoothness of the bathymetry or the magnitude of the deformation. We, therefore, prefer to use it over other more widely adopted approaches that involve incorporation of the horizontal motions approximately through computing the first-order Taylor expansion of Eq. **2** (18, 52, 53). Details of the tsunami model are given in *Materials and Methods*.

Results

Fig. 1 shows the development of the supershear rupture on a right lateral strike-slip fault in terms of fault slip rates and seafloor particle velocities. The earthquake nucleates at the hypocenter and propagates toward the free surface as it eventually saturates the seismogenic zone. The rupture first propagates at sub-Rayleigh speeds, before transitioning into the supershear mode.

Fig. 1*A* displays snapshots of the slip rate on the fault surface at different times. Initially ($t = 0.1$ s), we observe the nucleation of the earthquake within the overstressed region. Then, we observe the subsequent rupture expansion and the clear delineation of the rupture fronts, which continue to propagate toward the apex of the bay saturating the seismogenic zone ($t = 1.0$ s). As the rupture front reaches the top and bottom boundaries of the domain, waves are reflected back. At this stage, shock fronts start to develop on the fault surface, accompanying the transition to supershear propagation ($t = 2.0$ s), as we will discuss shortly in Fig. 1*B*. The shock fronts are capped by the locked-slipping interface at the bottom edge of the fault surface, resulting in another set of reflected waves ($t = 4.0$ s).

Fig. 1*A* also shows vectors of seafloor vertical particle velocity superimposed on the slip-rate snapshots to highlight a few observations: 1) The seafloor vertical velocity is highest in the vicinity of the rupture tip, as well as the trailing sub-Rayleigh wave front (all subplots); 2) pronounced vertical seafloor velocities accompany the supershear transition and the onset of the shock wave fronts ($t = 2.0$ s); 3) the vertical velocities continue to be high within the shock wave front region, as the rupture grows. Velocities elsewhere are diminished in comparison ($t = 4.0$ and 7.4 s). 4) The vertical velocities are not monotonic. They alternate between positive and negative values along the fault strike. The pronounced vertical velocity field, which persists around the rupture tip and within the shock wave region as the dynamic
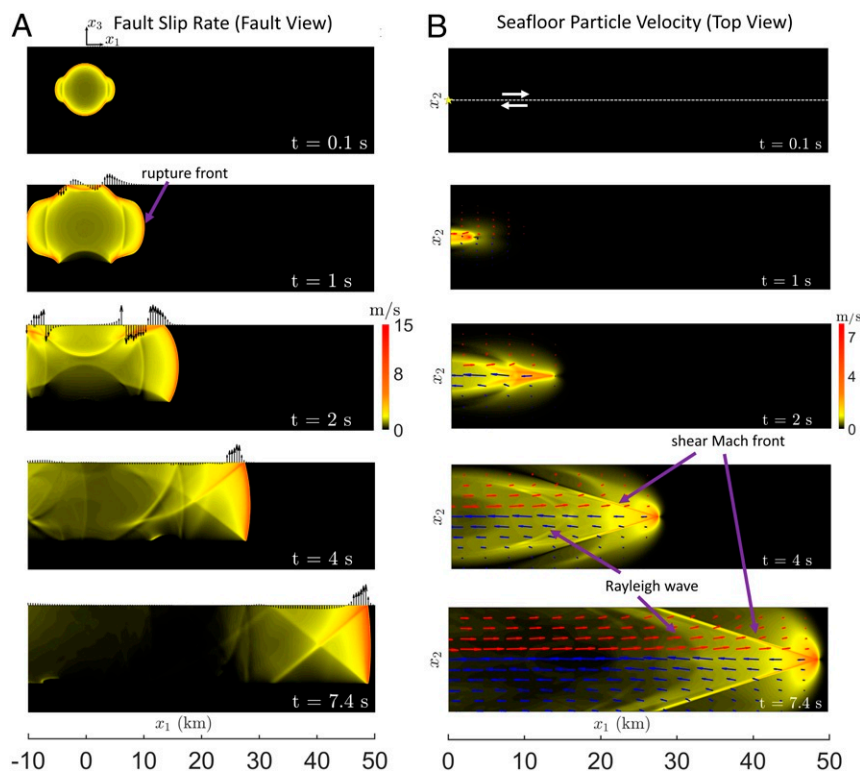
Fig. 1. Evolution of a supershear rupture on a right lateral strike-slip fault. Snapshots of the fault slip rate shown at times 0.1, 1.0, 2.0, 4.0, and 7.4 s (*A*) and seafloor particle velocity shown at times 0.1, 1.0, 2.0, 4.0, and 7.4 s (*B*), zooming onto the forward-propagating rupture tip ($x_1 \geq 0$). The position of the fault is indicated by the white dashed line ($x_2 = 0$) in the first panel of *B*, together with a pair of arrows highlighting the right lateral sense of the fault slip. On the fault plane, the rupture nucleates at depth within an overstressed region. It subsequently expands to reach the surface and propagates at supershear speeds after saturating the seismogenic zone. On the seafloor, shear shock wave fronts (Mach cones) emerge and sharpen, extending away from the fault with little attenuation, as the rupture continues to propagate. Vectors of the in-plane displacements are superimposed on the seafloor particle velocity contours to demonstrate the direction of the motion on the seafloor. The direction of these arrows is consistent with the right lateral slip motion on the fault surface. Vectors of the vertical seafloor velocity are superimposed on the slip-rate snapshots. Rupture features, such as the shear Mach cone and the trailing Rayleigh wave, are also highlighted. x_1 is the strike-parallel coordinate, x_2 is the strike-normal coordinate, and x_3 is the depth-wise coordinate.

rupture propagates, has a direct imprint on the generated tsunami, as will be discussed shortly.

Fig. 1*B* illustrates the magnitude of the particle velocity on the seafloor at different times, focusing on the forward-propagating rupture tip. Initially, there is no visible disturbance as the waves, emanating from the rupture at depth, have not reached the surface yet ($t = 0.1$ s). Then, as the rupture grows, parts of the rupture front reach the surface, and we observe the onset of intense ground motion ($t = 1.0$ s). As the rupture expands, we observe key characteristics of the supershear propagation, including 1) the sharp increase in the seafloor particle velocity during the rapid acceleration of the rupture from sub-Rayleigh to supershear speeds ($t = 2.0$ s); 2) the development of shear shock wave fronts, emerging due to the coherent interference of shear waves trailing the propagating rupture tip, which gradually extends into the bulk away from the fault ($t = 4.0$ s); 3) the development of a secondary Rayleigh wave front (36, 39, 44) that trails the shear shock wave front ($t = 4.0$ s); and 4) the sharpening of the shock fronts and their expansion into further distances within the bay, without significant attenuation ($t = 7.4$ s).

At all times, the rupture tip lags behind the dilatational wave front. The arrows in Fig. 1*B* represent the magnitude and direction of the resultant in-plane displacement. Since the fault slip has a right lateral sense, the seafloor is pushed away from the fault surface, on the top side of the forward-propagating rupture tip ("positive" side, $x_2 > 0$), while it is pulled toward the fault surface on the bottom side ("negative" side, $x_2 < 0$) ($t = 1.0$ s). As the rupture further expands, the magnitude of the in-plane displacements, reflected by the size of the arrows, increases, but the sense of motion just described above persists ($t = 2.0$, 4.0, and 7.4 s). These in-plane displacements are critical for the tsunami dynamics, as they may induce large seafloor bathymetric variations. In particular, if such a fault is traversing a bay, we expect that on the positive side of the fault, the slopes of the bay are

pushed landward ($u_1^s > 0$ and $u_2^s > 0$), which is equivalent to a downward movement of the seafloor. On the negative side of the fault, the slopes are pushed seaward ($u_1^s < 0$ and $u_2^s > 0$), which is equivalent to an upward movement of the seafloor. The equivalent vertical motion of the seafloor due to the bulk in-plane displacements is to be added to the direct vertical motion coming from the vertical displacements due to the strike-slip motion. The synergistic interaction between all of the displacement components enrich the tsunami dynamics, on different time scales, as we will discuss shortly.

We now turn our attention to the tsunami dynamics. Fig. 2*A* illustrates the bathymetry of the simulated bay. The bay geometry is partially inspired by the geometry of the Palu Bay. The Palu Bay has a narrow (width ~ 8 km) and shallow (maximum depth ~ 700 m) trench with a rounded apex at the end (54). Here, we also consider a generic, narrow, and shallow bay with a rounded apex as an example of this class of geometries. The exact dimensions of our geometry are given in *SI Appendix,* section S2. We record the water-surface amplitude at a number of stations located at various locations within the bay (along section A-A) and along the coastline. We note that a spectrum of time scales emerges for near-source tsunamis, like the one modeled here, which is usually overlooked in the more commonly studied far-source tsunamis. Specifically, we define:

1. An instantaneous dynamic tsunami phase (on the scale of few seconds, as shown in Fig. 2 *B–D*), in which the water surface is directly, and almost instantaneously, driven by the coseismic motion of the seafloor ($H_{,t} \neq 0$), even at large distances from the fault plane, because of the unattenuated action of the shock waves.
2. A coseismic tsunami phase that is initiated by the dynamic seafloor motion adjacent to the fault, but propagates slower than the dynamic one, due to the diminishing effect of the
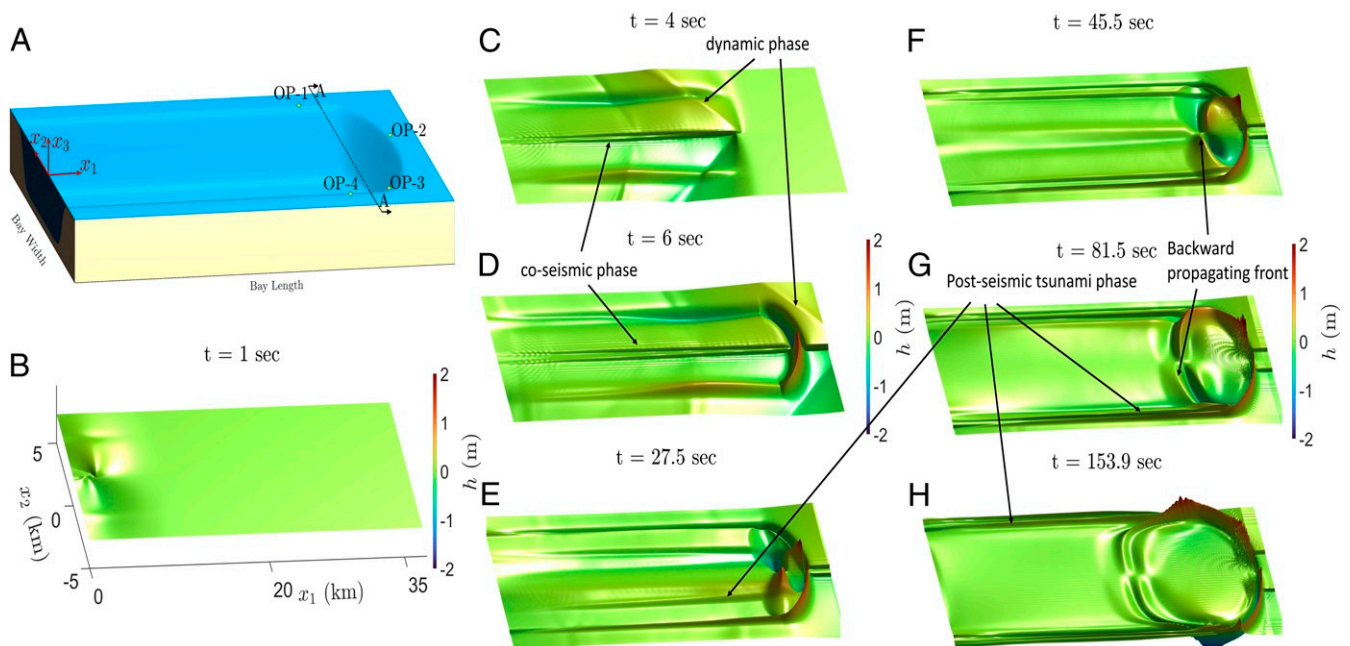

Fig. 2. Evolution of the earthquake-induced tsunami in a bay traversed by a supershear rupture. (*A*) Bay bathymetry, with the various observation stations (OP) and section A-A marked. The right-handed Cartesian coordinate system is also shown for reference. (*B–H*) Snapshots of the supershear tsunami scenario at times 1.0, 4.0, 6.0, 27.5, 45.5, 81.5, and 153.9 s, shown sequentially from left to right. Colors indicate the sea-surface height (*h*) relative to the undisturbed water level. *B–D* correspond to the "dynamic tsunami-generation phase." *E–G* correspond to the "postseismic tsunami-generation phase." The evolution of different tsunami-generation mechanisms, as well as coseismic rupture signatures, are observed. Note the common color-scale bar between all of the subplots. An alternative representation for these surface plots, in which multiple scale bars, adjusted for the local water-surface peak amplitude in each displayed time step, is provided in *SI Appendix,* Figs. S1 and S2

$H_{,t}$ term, as the rupture front zips along the fault plane (as shown in Fig. 2 *B–D*). This phase can be described as two water waves with crests along the fault strike-parallel direction (x_1 direction) moving in the strike-normal direction (x_2 direction).

3. A much slower, postseismic tsunami (on the scale of tens of seconds to several minutes, as shown in Fig. 2 *E–H*) that emerges after all elastodynamic waves have exited the simulated domain. This phase is driven by gravity and is prone to reflection, refraction, and amplification by the bay geometry.

While the postseismic tsunami is set in motion by the history of both the dynamic and coseismic tsunami phases, its propagation has no input from the time-dependent motion of the bathymetry ($H_{,t} = 0$). In the case of far-field tsunamis, the postseismic tsunami occurs on the scale of tens of minutes to hours. Therefore, neglecting the initial dynamic phase, which occurs on the time scale of seconds, may be justified.

Fig. 2 *B–D* show the dynamic, and coseismic, tsunami-generation phases commensurate with the earthquake nucleation and subsequent propagation. Since the rupture speed is nearly two orders of magnitude larger than the speed of gravity sea-surface long waves, there is a negligible effect of shallow-water dispersion during the dynamic tsunami wave, and the tsunami dynamics are entirely dominated by the rapid variation in the seafloor topography. This is why we almost immediately observe features in the water-surface profile that are identical to the features reported for the seafloor deformation from the earthquake simulation, including the shock wave fronts and the trailing Rayleigh wave pulse. These features also reflect the strong signature of the seafloor vertical velocity highlighted in Fig. 1*B*.

Furthermore, Fig. 2 *C* and *D* show that the horizontal motion of the bathymetry due to the ground motion profile (highlighted in Fig. 1*B* during the dynamic rupture) results in a pronounced variation in the water surface at the banks of the bay. These are recognized by the ridge-like features that very quickly form local water disturbances that emerge on both sides of the bay. Moreover, as the strike-slip rupture further propagates, we observe the emergence of secondary water wave fronts that join at the rupture tip and form a very shallow angle with the fault strike-parallel direction. These fronts belong to the coseismic tsunami phase, which subsequently propagates away from the fault at speeds proportional to $\sqrt{gH}$ as part of the gravity-driven, postseismic tsunami. The postseismic tsunami phase commences once the magnitude of the ($H_{,t}$) term becomes negligible as the dynamic rupture exits the simulation domain.

Fig. 2 *E–H* further demonstrate the postseismic tsunami onset and propagation, as well as its interaction with the apex region. The tsunami waves that emanate from the fault surface, as described above, propagate in the strike-normal direction toward the coastlines on both sides of the bay. These waves have an initial amplitude set by the vertical displacement at the seafloor due to the earthquake. While strike-slip faults generate predominantly horizontal displacements, there still is a nonnegligible vertical component that emerges at the seafloor to satisfy the plane stress condition at the solid earth free surface. This is true, especially when these ruptures are supershear, in which case this out-of-plane displacement is not localized at the rupture tip, but extends along the Mach fronts (45, 55).

Simultaneously, gravity-driven tsunami waves start to evolve over the banks of the bay. These waves are created following the initial dynamic disturbance that resulted from the coupling between the horizontal motion of the bathymetry and the uplift/depression of the sea surface. We observe that this initial disturbance is dispersed into two waves, one traveling toward the center of the bay and the other toward the coast. The coast-heading waves are a direct threat for the coastal community.

In the apex region, the water wave amplitude reaches 2.47 m and persistently propagates through the shallow portion of the coastline without much attenuation. We note that these waves form on time scales of tens of seconds, and it takes only a couple of minutes to cover hundreds of meters overland beyond the shoreline. This highlights the unique hazard poised by this type of tsunamis, as they allow very little time for early warning.

Another remarkable phenomenon relates to the reflection and refraction of the tsunami waves as they interact with the apex region. We observe that the high-amplitude initial disturbance, set by the dynamic displacements of the slopes at the apex, travels radially backward toward the interior of the bay, hitting coastal regions located further back. The amplitude of these reflected waves continue to grow as they propagate backward due to the amplification by the shoreline bathymetry and interaction with other waves existing in the bay. The complex water wave pattern that emerges from the simple bay geometry and simple earthquake-source characteristics highlights the importance of considering the strike-slip horizontal motions when modeling tsunami hazard in narrow bays. Specifically, the interaction of the rupture dynamics, and the full 3D displacement field, with the bay slopes may contribute to substantial amplification in the water wave amplitudes, even in the absence of triggered landslides.

To gain further insights into the characteristics of these different tsunami-generation mechanisms, we investigate the spatio-temporal evolution of the water level. Fig. 3 shows snapshots of the water level along section A-A, located at $x_1 = 29.5$ km (shown in Fig. 2*A*), during the dynamic, coseismic, and postseismic tsunami-generation phases, respectively. Several observations follow. Within the dynamic tsunami-generation phase ($t = 6.0$ s), we observe the emergence of a nonnegligible disturbance in the water-surface profile close to the fault location, highlighted by one of the red arrows in Fig. 3*A*, corresponding to the vertical seafloor displacements carried by the shock fronts. The coupling between the horizontal motion of the sides of the bay and the vertical displacement of the sea surface leads to the emergence of an instantaneous pronounced crest and valley in the water-surface profile over the right ($x_2 < 0$) and left ($x_2 > 0$) banks, respectively. The valley is highlighted by the other red arrow in Fig. 3*A*. Subsequently, each of these initial disturbances results in two propagating fronts, one expanding in the direction of the coast and the other toward the center of the bay, as detailed in the insets in Fig. 2 over the time period $t = 8.0$ to 12.0 s. The speed of the fronts is governed by the varying water depth. The front propagating toward the center of the bay travels faster. At $t = 25.0$ s, the front propagating toward the center of the bay coalesces with the tsunami wave propagating away from the fault surface toward the coastline, to form a larger-amplitude wave.

Fig. 3*B*, whose vertical scale has been adjusted by a factor of three compared to Fig. 3*A*, highlights the postseismic tsunami-generation phase. The postseismic tsunami waves (marked by the white arrow) propagate further toward the coast, while the radially traveling wave front from the apex (marked by the black arrow and shown in the contour plots to the right) expands further toward the coast. A sudden increase in the water level is observed as the radially traveling wave front approaches the coastline due to amplification by the diminishing water depth. We observe that these high-amplitude waves emerge at different focal points, long past the initial disturbance of the water level, and constitute a substantial hazard for the bay coastlines. It is important to note that the solution is not antisymmetric about the fault surface. This deviation is most obvious at $t = 120.0$ s, where the magnitude of the water level is higher on the right side of the bay ($h = -1.6$ m) compared to the left side ($h = 1.3$ m). The lack of perfect antisymmetry is explained by the symmetric nature of the strike-normal seafloor horizontal displacement u_2^s, while the other two components of seafloor
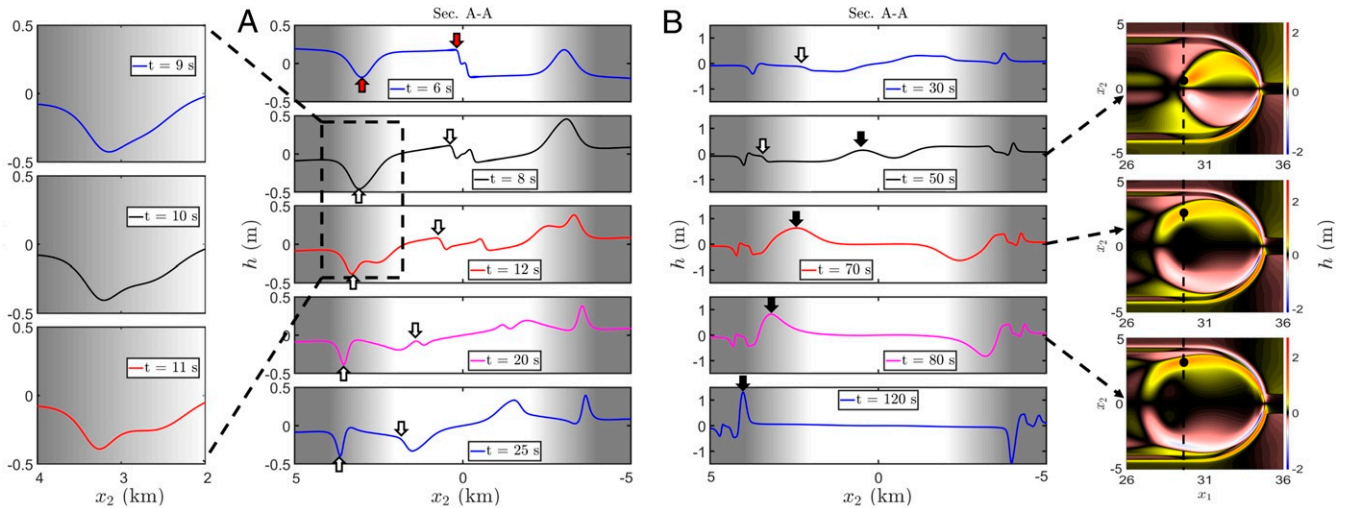
Elbanna et al.
Anatomy of strike-slip fault tsunami genesis

PNAS | 5 of 11
https://doi.org/10.1073/pnas.2025632118

Fig. 3. Snapshots of sea-surface height *h* for cross-section A-A. The snapshots correspond to different phases of tsunami generation associated with different time scales. (*A*) Late dynamic tsunami phase to early postseismic phases at times 6, 8, 12, 20, and 25 s. (*B*) Fully developed postseismic tsunami phase at times 30, 50, 70, 80, and 120 s. Grayscale indicate the bathymetry variation along the cross-section where the depth varies from 700 to 10 m over a distance of 2 km. The instantaneous dynamic phase is marked by red arrows. The postseismic tsunami waves are marked by white arrows. The postseismic radially traveling wave front from the apex is marked by black arrows. These phases are highlighted for $x_2 \geq 0$, but a similar pattern exists for $x_2 \leq 0$. The evolution of the early phases of the postseismic tsunami waves over the banks of the bay is emphasized in the zoomed-in plots in the left column. Contour plots (*Right*) show the reflected and refracted tsunami waves, which are also part of the postseismic tsunami phase, propagating backward from the apex toward cross-section A-A. The black arrows in *B* correspond to the black dots in the contour plots in the rightmost column. A more detailed breakdown for the dynamic tsunami-generation phase between times $t = 4.0$ s and $t = 7.5$ s is provided in *SI Appendix*, Fig. S3.

displacement u_1^s, u_3^s are antisymmetric. This is consistent with the field observations of Fritz et al. (56).

In Fig. 4, we show snapshots of the in-plane water-particle velocity as vectors superposed on the water-surface height during the different tsunami-generation phases. Fig. 4*A* shows that the arrival of the rupture tip at the apex, at $t = 6.0$ s, leads to an abrupt variation in the water-surface level. Since the fault slip is right lateral, the flat portions of the seafloor would move up on the positive side ($x_2 > 0$) of the fault, and down on the negative side ($x_2 < 0$) of the fault. This causes the water-particle velocity to be pointing downward (from higher to lower water-surface elevations) along the segments of the fault not traversing the coastline slopes. In the meantime, within the apex region, this right lateral motion pushes the shoreline landward on the positive side of the fault surface, but pushes it seaward on the negative side. As a result, the water surface is depressed on the positive side, while it is elevated in the negative side. This causes the water-particle velocity in the apex region to point upward along the x_2 direction. As highlighted in the zoomed plot in Fig. 4*A*, this direction of water-particle velocity in the apex region is opposite to the direction of the water-particle velocity in the rest of the water surface along the fault line ($x_2 = 0$).

Fig. 4*B* shows snapshots of the in-plane water-particle velocity at a later time ($t = 45.5$ s), well within the postseismic tsunami phase. Several observations follow in this case: 1) The particle velocity within the deeper portion of the apex region points predominantly in the strike-normal direction from the negative side of the fault to the positive side. This sense of motion is the result of the motion of the banks of the bay due to the horizontal displacements of the strike-slip fault. Specifically, the bay slopes on the negative side are pushed seaward, while those on the positive side are pushed landward. This leads to the water body having a momentum component, in the strike-normal direction, pointing from the negative to the positive sides of the fault. 2) The backward-propagating fronts that are reflected from the apex locally modify the direction of the in-plane particle velocity (Fig. 4*B*; zoom in *A*). Specifically, we observe an anticlockwise

sense of motion that seems consistent with the particle velocity pointing from regions of higher to lower water-surface elevations behind the backward-propagating reflected front. In the region where the water surface is unperturbed ($h = 0$), the particle velocity maintains its strike-normal direction, as discussed above. 3) In the shallower parts of the apex region, we observe that the forward-propagating wave (moving up the slope) is compressed, while the backward-propagating wave (moving down the slope) is rarefied. This is accompanied by an increase in the water in-plane particle velocity in both forward and backward directions at the edge of the basin (Fig. 4*B*, zoom in *B*). The water in-plane particle velocities are of the order of 1 m/s, which may be significant enough to impact the morphology of the shoreline (57).

Fig. 4*C* shows further evolution of the in-plane water-particle velocities at a later time. We observe differences in the magnitude of the particle velocity at the lateral sides of the bay. Specifically, the particle velocity over the bay banks on the negative side of the fault is 1.375 times larger the particle velocity on the positive side. This may be explained as follows. On the negative side of the fault, the water-particle velocity is amplified. This is due to the constructive interference of the reflected water wave from the apex and the increased water-surface height generated from the seaward motion of the side of the bay. On the positive side of the fault, the water-particle velocity is reduced. This is due to the destructive interference between the reflected wave from the apex and the decreased water-surface height generated from the landward motion of the side of the bay. This variation in interaction patterns between the different waves propagating within the basin intensifies the contrast in the particle-velocity amplitudes at the two sides of the bay.

We also examined tsunami generation in a bay traversed by a sub-Rayleigh rupture. The simulation domains for the tsunami and earthquake models have identical material properties and dimensions in both the sub-Rayleigh and supershear cases. To generate a sub-Rayleigh rupture, we reduce the value of the initial shear stress, as outlined in *Materials and Methods*.
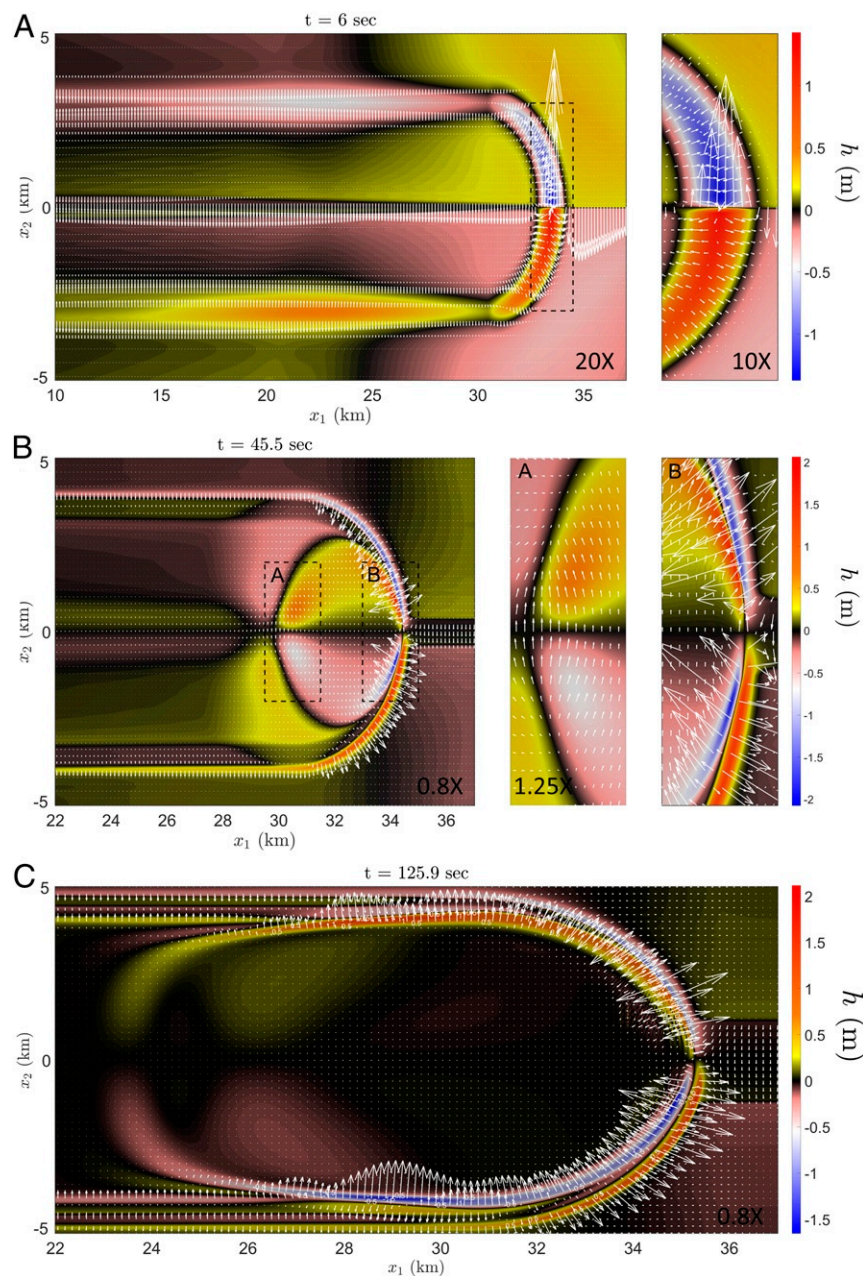
Fig. 4. Snapshots of the in-plane water particle velocity vectors at different phases of tsunami generation. Colors indicate the sea-surface height h relative to the undisturbed water. (*A*) The dynamic tsunami-generation phase at $t = 6.0$ s. The vector magnitudes are scaled by a factor of 20 for representation. (*B*) The postseismic tsunami phase at 45.5 s, highlighting the structure of water motion near the apex of the bay. The vector magnitudes are scaled by a factor of 0.8 for representation. (*C*) The postseismic tsunami phase at 125.9 s, revealing the coalescing wave fronts and highlighting the lack of perfect antisymmetry between the two sides of the bay. The vector magnitudes are scaled by a factor of 0.8 for representation.

Fig. 5 illustrates the time history of the water-surface amplitude for both rupture profiles at the different stations shown in Fig. 2*A*. For the supershear rupture, at station OP-1, located at $(x_1, x_2) = (27.5, 4)$ km shown in Fig. 5*A*, the passage of the shock wave front causes an abrupt uplift of water surface of amplitude 0.26 m at time $t = 5.1$ s. Following this uplift, the water level is depressed, corresponding to the arrival of the tsunami wave front that ensued from the horizontal displacement of the slope (up to $t \sim 50.0$ s); see also Fig. 3. This is followed by another postseismic tsunami wave that leads to water resurgence ($t \sim 1.0$ min). Finally, the high-amplitude wave from the radially propagating front, which is reflected from the apex and further refracted by

the bay geometry, arrives at around $t = 2.25$ min. Due to the absence of shock waves in the sub-Rayleigh case, we observe a much smaller dynamic tsunami pulse of the order of 0.09 m at time $t = 10.0$ s, which is associated here with the passage of the Rayleigh wave. This is further highlighted in Fig. 5 *A*, *Inset*. The postseismic tsunami features are similar across the supershear and sub-Rayleigh cases, except that the amplitudes in the sub-Rayleigh case are smaller and vary more gradually.

Fig. 5*B* illustrates the water-surface dynamics at station OP-2, located near the apex of the bay at $(34.5, 1)$ km. Again, we observe an increase in the water level of 0.24 m at time $t = 6.0$ s, corresponding to the dynamic excitation by the passage of the
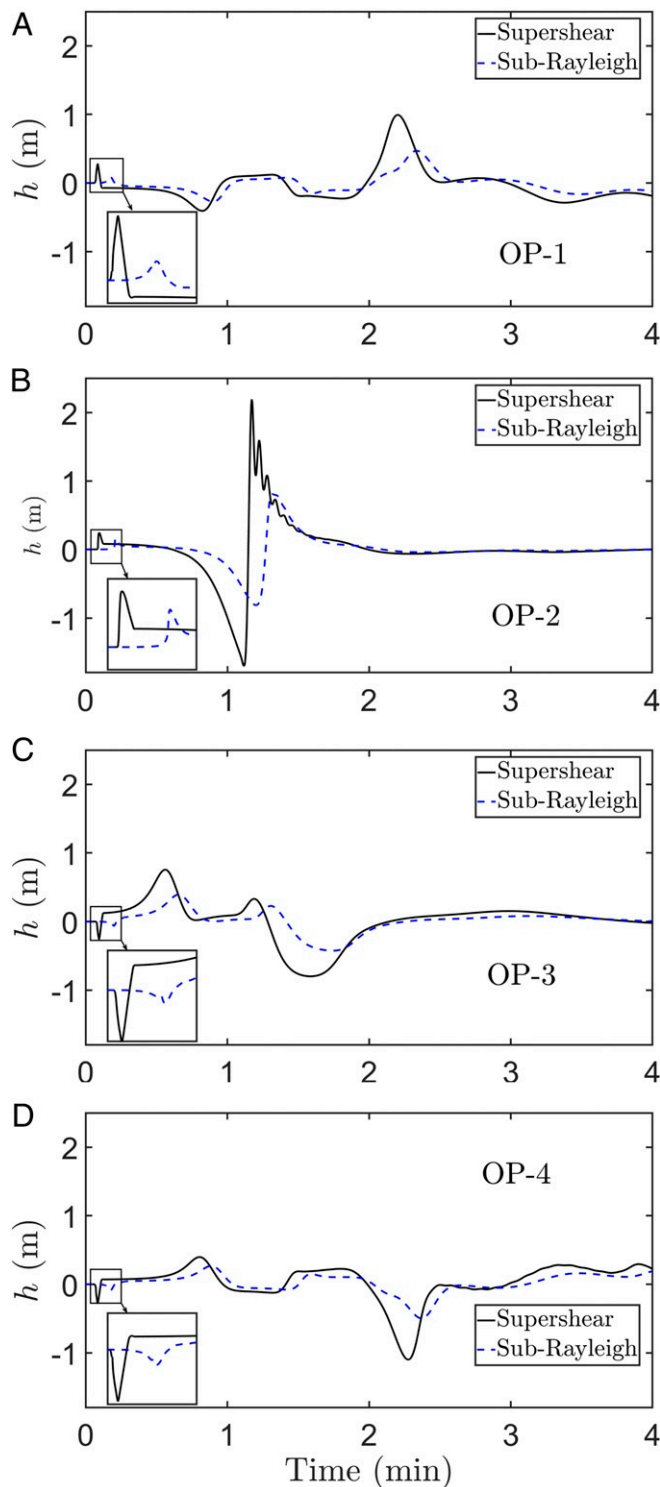
Elbanna et al.
Anatomy of strike-slip fault tsunami genesis

PNAS | 7 of 11
https://doi.org/10.1073/pnas.2025632118

Fig. 5. Comparison between water-level time histories corresponding to a supershear and a sub-Rayleigh rupture traversing the same bay. Time histories obtained for the tsunami at stations OP-1 (*A*), OP-2 (*B*), OP-3 (*C*), and OP-4 (*D*) are shown. The locations of the stations are shown in Fig. 2*A*. Black solid lines correspond to water-surface height associated with supershear rupture. Blue dashed lines correspond to water-surface height associated with the sub-Rayleigh rupture. The arrival of dynamic, rupture-induced water wave is highlighted in the zoomed portion. A modified version of this figure, in which the water-level time history is scaled by the average slip in each rupture scenario, is presented as *SI Appendix*, Fig. S4.

shock waves. This is followed by a large-amplitude depression of (-1.7 m) at $t \sim 1.1$ min. Subsequently, a rapid increase in the water surface is observed, with the maximum water-level height reaching 2.174 m at $t \sim 1.25$ min. While we do not attempt to model Palu Bay explicitly, it is interesting to note that Palu city is located exactly at the apex of the Palu Bay, and this is where our simulation predicts the largest amplification in the water level. The rapid variation in the water-level amplitude (4 m) from depression to resurgence, occurring over a time span of just 0.15 min, is only observed at this location and may have important implications for liquefaction potential.

On the other hand, the sub-Rayleigh case shows a smaller range of variation in the water-level amplitude, as low as half the corresponding amplitude in the supershear case. In both cases, we observe the emergence of multiple oscillations trailing the peak wave. These oscillations are artifacts of the numerical discretization of the shallow-water wave equations using low-order finite elements. The reader is referred to *SI Appendix*, section S2 for further discussion on the nature of these oscillations. Specifically, *SI Appendix*, Fig. S5 demonstrates that the amplitude and wavelength of the trailing oscillations, observed in the water level at OP-2, are reduced when the mesh is refined. This, however, comes at a significant computational cost. The main features, such as the peak amplitude and arrival times, show convergence and are consistent at different element sizes.

At the other side of the bay, Fig. 5*C* shows the time history for station OP-3 at $(31.5, -3.65)$ km. The dynamic disturbance from the passage of the dynamic rupture is observed at $t = 5.7$ s and is manifested in the local water-surface depression of amplitude 0.257 m. After half a minute, we observe the tsunami wave associated with the slope motion, followed by the near-fault tsunami wave, and, finally, the radially propagating front arrival. All of the key features are observed at an earlier arrival time than station OP-1, due to the proximity of station OP-3 to the apex. Finally, Fig. 5*D* presents the time history of water level at station OP-4, which mirrors station OP-1 in location. Accordingly, the time history is similar, but with opposite polarity, consistent with the sense of motion on the fault and subsequent displacement of the slopes.

The smaller amplitude of tsunami waves in the sub-Rayleigh case is attributed mainly to the smaller vertical and strike-parallel seafloor displacements u_3^s, u_1^s, respectively. The effect of smaller vertical displacements is evident in the absence of a strong dynamic tsunami pulse. The weaker strike-parallel seafloor displacement leads to diminished bathymetric motions at the apex, resulting in substantially lower uplifts and reduced water wave amplitudes.

These observations have two major implications. First, for a given fault area, a tsunami generated by a supershear earthquake will be larger than that generated by a sub-Rayleigh one. Second, the difference between the two tsunamis is not simply a matter of scaling the sub-Rayleigh rupture to generate a slip equal to the supershear one. If it was an issue of scaling, the ratio between the time histories in the two cases would have been the same throughout. Rather, it is evident that different features in the time histories from the two tsunamis have different relative amplitudes. For reference, the maximum slip in the simulated supershear rupture is 8.4 m, while the corresponding value in the sub-Rayleigh rupture is 6.3 m. However, the tsunami waves generated by the supershear rupture have amplitudes at peak values that range between one and four times as large as the one generated by the sub-Rayleigh one. This suggests that there exists a synergistic effect between the details of the dynamic rupture in both modes, the relative amplitude of strike-parallel and strike-normal components of displacements, the motion of the bathymetry, and the subsequent water-level motion.

Furthermore, *SI Appendix*, Fig. S5 displays the water-level time history scaled by the average slip for each of the rupture scenarios.

The scaled figure shows that the difference in slip does not completely explain the difference in the changes in the water-level profile as a function of time, nor the amplitude difference.

To emphasize the role of horizontal displacements on the induced tsunami, we compare the supershear earthquake-induced tsunami for three cases: 1) in a bay with all of the three components of the seafloor motion contributing to the bathymetry deformation; 2) in a bay with only the vertical component of the seafloor motion being considered; and 3) in an open ocean with a flat bathymetry of constant depth.

Fig. 6*A* illustrates the response at station OP-1 in the three cases. For case 1, in which all components of motion are considered, we observe the arrival of the dynamic tsunami phase, then a coseismic tsunami phase, followed by the postseismic tsunami wave, and then the radially propagating front that is reflected from the apex and subsequently refracted by the bay geometry. On the contrary, the time history for case 2, in which only the vertical component of seafloor motion is included, indicates a weak tsunami signal. The dynamic tsunami signature, associated with the passage of the shock waves on the seafloor, is identical to that observed for case 1. However, the subsequent postseismic tsunami is much smaller than in case 1.

The postseismic tsunami in case 2 is generated by the waves set up at the fault with an amplitude determined by the residual displacements from the 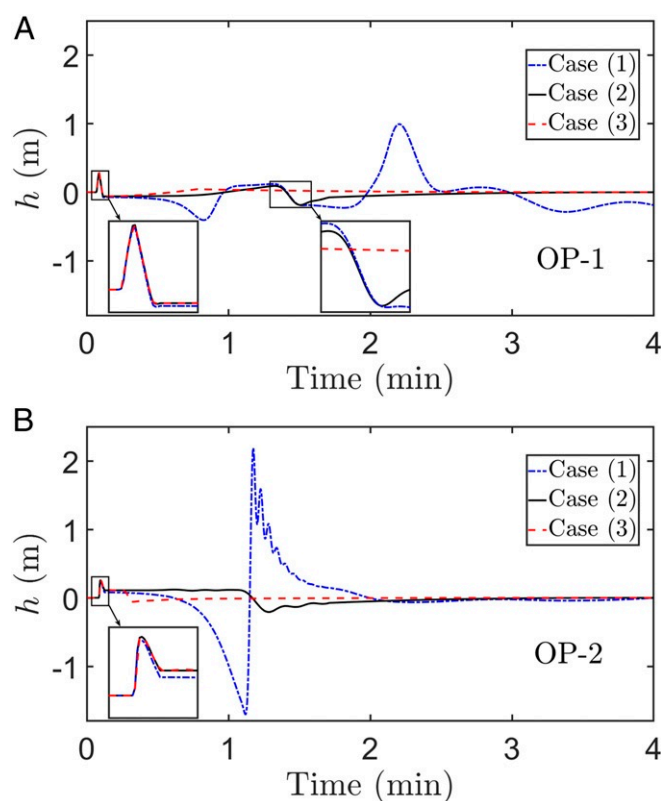dynamic rupture. These waves have relatively small amplitude and are only weakly amplified as they run up the slope. For comparison, we also include the time history for the water-surface amplitude in case 3, where the depth is uniform. In this case, we again see an identical signature of the dynamic tsunami corresponding to the passage of the shock wave fronts. This is then followed by the postseismic tsunami wave set up by the residual displacement field near the fault surface. Unlike cases 1 and 2, these waves are not amplified further, since the water depth is uniform. The waves simply pass by the observation station, and the recorded water-level amplitude subsequently decays to zero.

In the absence of horizontal motion, Fig. 6*B* further demonstrates that there is no substantial water uplift or depression. This is possibly the reason conventional tsunami models, which only include vertical seafloor displacements, do not generate sizable surface waves. Hence, this type of generation mechanism has been overlooked and this is particularly problematic for probabilistic tsunami hazard analyses, which anyway do not include the effects of slow earthquakes. In the presence of horizontal displacements, the tsunami wave height may reach few meters, and the water sea surface may change rapidly over a few seconds.

These observations point to the critical role of horizontal motions in tsunami generation by strike-slip faults. The large horizontal motions characteristic of supershear earthquakes (36, 39) on long strike-slip faults may cause significant displacement to the coastline or bay bathymetry, leading to vertical displacements of the water surface that may not be insignificant compared to those resulting from normal faulting. Strike-slip faults traversing narrow bays or heading toward coastlines may thus pose a significant tsunami hazard, even in the absence of landslides.

Conclusions

Our results suggest that strike-slip faults, unlike what is typically assumed (15, 58, 59), may cause large tsunamis without the need to trigger underwater landslides. These results are based on numerical simulations of simple dynamic rupture scenarios on planar faults traversing a bay with idealized and smooth geometry. In that respect, our results are not masked by complex topography or complicated ground motions. Rather, they reveal some intrinsic mechanisms through which strike-slip faults may become tsunamigenic.

Our model identifies several distinct features of tsunamis generated by strike-slip faults traversing narrow bays. Notably, we recognize three distinct phases in the associated wave motions: 1) an instantaneous dynamic phase that is advected by the elastodynamic field emanating from the dynamic rupture. The speed of propagation of this phase is several kilometers per second, and, hence, it reaches the coastal areas synchronously with the shaking. 2) A coseismic tsunami phase emerges while the dynamic rupture is still active, but propagates at a slower speed than the dynamic tsunami phase, due to the diminishing effect of seafloor velocities with time; and 3) a gravity-driven postseismic phase, which takes tens of seconds to several minutes to affect the coastal region. This phase, which carries memory of the histories of both the dynamic and coseismic tsunamis, is probably the most hazardous of the three phases due to its propensity to focusing effects at the apex, reflection and refraction by the bay geometry, and amplification by the bathymetry. The classification of tsunami motions we are introducing here may be potentially helpful in deciphering the multiple time scales observed in near-source tsunami records and unexplained field observations.

Strike-slip faults usually generate large horizontal displacements, but limited vertical displacements. It turns out that the positioning of the strike-slip fault with respect to the coastline is critical in leveraging these larger horizontal displacements in tsunami generation. Specifically, if the strike-slip fault is located near the shore and is positioned such that it traverses a bay area or is heading toward the coastline, the tsunami hazard is

Fig. 6. The effect of including the horizontal motion on a basin bathymetry for a bay traversed by a supershear rupture. The blue dash-dot line corresponds to the water-level time history when all motions are included (case 1). The solid black line shows the water-level time history when horizontal motions are excluded (case 2) The red dashed line shows the water-level time history in the open ocean with a flat bathymetry of constant depth (case 3). The time histories are shown at stations OP-1 (*A*) and OP-2 (*B*). The dynamic tsunami phase at both stations is highlighted within the zoomed plots. A segment of the postseismic tsunami phase at station OP-1 around $t \sim 90.0$ s is also highlighted in an inset. The locations of the stations are shown in Fig. 2*A*.

Elbanna et al.
Anatomy of strike-slip fault tsunami genesis

PNAS | 9 of 11
https://doi.org/10.1073/pnas.2025632118

amplified. The presence of an apex at the tip of a bay further enhances this effect, since it results in wave focusing, reflection, and refraction, enabling multiple interactions with the slopes of the bay. The reason for this phenomenon is that in such geometries, the strike-normal and strike-parallel components of ground motion will cause horizontal deformations in the shoreline slopes, which, in turn, lead to vertical displacement of the water surface. If the slopes are steep enough, the resulting disturbance in the water surface may be significant. While the effect of coupling between the horizontal motion and water-level uplift has been recognized for tsunamis induced by subduction zone earthquakes (60–62), it has not been appropriately considered for strike-slip faults. We note that this effect may be nonnegligible, and overlooking it in the case of strike-slip faults may lead to gross underestimation of the associated tsunami hazards.

Another important conclusion of our work is that the details of rupture propagation matter. Supershear ruptures are capable of generating larger tsunamis than sub-Rayleigh ruptures for the same rupture area. The shock wave fronts, which emerge during supershear propagation, carry in-plane and out-of-plane dynamic seafloor displacements and velocities to large distances away from the fault without significant attenuation (34, 38, 39). They are also more efficient in focusing energy ahead of the rupture tip and along the direction of propagation. These focused unattenuated displacements result in a stronger interaction between the dynamic earthquake motion and shoreline bathymetry, especially at the apex of bays, during the dynamic and coseismic phases of the tsunami. This, in turn, sets up higher water-surface displacements, which subsequently get further amplified as they run up the slopes.

While for the same fault area, sub-Rayleigh ruptures produce smaller slip than supershear ruptures, the reduction in slip alone does not explain the smaller tsunami wave heights in the sub-Rayleigh case. Rather, our results suggest that the full history of the source dynamics, which also result in different spatial distributions of the final slip and ground motions, is critical to explain such discrepancy. This further motivates the need for integrated dynamic rupture–tsunami models like the one adapted here.

Since our modeling has used generic features of the earthquake and tsunami sources, we expect that our results are not per se location-specific. Supershear rupture propagation, other similar bay geometries, and horizontal displacements of shoreline slopes all may combine to produce tsunami amplification from strike-slip faults in different geographic areas. Potential candidates include the San Francisco Bay and the Tomales Bay in Northern California, crossed by the San Andreas Fault; Izmit bay in Turkey, crossed by the North Anatolian Fault; and Al-Aqaba bay in Egypt, crossed by the Dead Sea Transform fault system. Just as in Palu Bay, tsunamis have been reported in these regions in the past (22, 63–66), and some of these faults have also had supershear rupture earthquakes (19, 67, 68). We, thus, recommend revisiting the tsunami risks associated with large submarine strike-slip faults, particularly those traversing narrow bays, with extraordinary caution needed in interpreting probabilistic hazard analyses which have not included strike-slip events in aggregating the hazard.

Materials and Methods

We used the crustal-deformation finite-element software PyLith for the earthquake rupture simulations. PyLith has been verified by using community-driven benchmarks, which are in line with Southern California Earthquake Center/US Geological Survey Dynamic Rupture Code Verification exercises, and it can be obtained at https://geodynamics.org/cig/software/pylith (69). More details on the elastodynamic governing equations and simulation parameters are available in *SI Appendix*, section S1. The tsunami simulations were run by using SWIM, an in-house partial differential equation solver built on the MOOSE framework (70). This nonlinear solver discretizes the shallow-water equations spatially by using the finite-element method and implicit time stepping for time integration. The tsunami is generated by the time-dependent motion of the bathymetry imported from the 3D dynamic rupture model in PyLith. A more detailed description of the tsunami model setup is given in *SI Appendix*, section S2. Furthermore, we have verified SWIM using several benchmark problems in the literature (71–73). An example of the verification is presented in *SI Appendix*, section S3.

Data Availability. All study data are included in the article and/or supporting information.

1. U. Kânoğlu, V. Titov, E. Bernard, C. Synolakis, Tsunamis: Bridging science, engineering and society. *Phil. Trans. Math. Phys. Eng. Sci.* **373**, 20140369 (2015).
2. C. E. Synolakis, E. A. Okal, "1992–2002: Perspective on a decade of post-tsunami surveys" in *Tsunamis*, K. Satake, ed. (Advances in Natural and Technological Hazards Research, Springer-Verlag, Berlin, Germany), vol. 23, pp. 1–29.
3. K. Satake, E. A. Okal, J. C. Borrero, "Tsunami and its hazard in the Indian and Pacific Oceans: Introduction" in *Tsunami and its Hazards in the Indian and Pacific Oceans*, K. Satake, E. A. Okal, J. C. Borrero, eds. (Birkhäuser Basel, Basel, Switzerland, 2017), vol. 110, pp. 249–259.
4. M. R. Legg, J. C. Borrero, C. E. Synolakis, Tsunami hazards from strike-slip earthquakes (abstract). *AGU Fall Meeting Abstracts* 2003, OS21D–06 (2003).
5. M. Carvajal, C. Araya-Cornejo, I. Sepúlveda, D. Melnick, J. S. Haase, Nearly instantaneous tsunamis following the M_W 7.5 2018 Palu earthquake. *Geophys. Res. Lett.* **46**, 5117–5126 (2019).
6. A. Muhari, F. Imamura, T. Arikawa, A. R. Hakim, B. Afriyanto, Solving the puzzle of the September 2018 Palu, Indonesia, tsunami mystery: Clues from the tsunami waveform and the initial field survey data. *J. Disaster Res.* **13**, sc20181108 (2018).
7. Y. Altinok et al., The tsunami of August 17, 1999 in Izmit Bay, Turkey. *Nat. Hazards* **24**, 133–146 (2001).
8. A. C. Yalciner et al., Tsunami waves in Izmit Bay. *Earthq. Spectra* **16** (suppl. A), 55–62 (2000).
9. C. E. Synolakis et al., The slump origin of the 1998 Papua New Guinea Tsunami. *Proc. R. Soc. Lond. Ser. A: Math. Phys. Eng. Sci.* **458**, 763–789 (2002).
10. S. Tinti, E. Bortolucci, C. Chiavettieri, Tsunami excitation by submarine slides in shallow-water approximation. *Pure Appl. Geophys.* **158**, 759–797 (2001).
11. F. Imamura et al., Field survey of the 1994 Mindoro Island, Philippines tsunami. *Pure Appl. Geophys.* **144**, 875–890 (1995).
12. S. Sassa, T. Takagawa, Liquefied gravity flow-induced tsunami: First evidence and comparison from the 2018 Indonesia Sulawesi earthquake and tsunami disasters. *Landslides* **16**, 195–200 (2019).
13. H. Bao et al., Early and persistent supershear rupture of the 2018 magnitude 7.5 Palu earthquake. *Nat. Geosci.* **12**, 200–205 (2019).
14. A. Socquet, J. Hollingsworth, E. Pathier, M. Bouchon, Evidence of supershear during the 2018 magnitude 7.5 Palu earthquake from space geodesy. *Nat. Geosci.* **12**, 192–199 (2019).
15. E. Oral, H. Weng, J. P. Ampuero, Does a damaged-fault zone mitigate the near-field impact of supershear earthquakes?—Application to the 2018 M_w 7.5 Palu, Indonesia, earthquake. *Geophys. Res. Lett.* **47**, 1–9 (2020).
16. K. Nakata, A. Katsumata, A. Muhari, Submarine landslide source models consistent with multiple tsunami records of the 2018 Palu tsunami, Sulawesi, Indonesia. *Earth Planets Space* **72**, 44 (2020).
17. A. L. Williamson, D. Melgar, X. Xu, C. Milliner, The 2018 Palu tsunami: Coeval landslide and coseismic sources. *Seismol. Res. Lett.* **91**, 3148–3160 (2020).
18. T. Ulrich et al., Physics-based modeling reveals earthquake displacements are critical to the 2018 Palu, Sulawesi tsunami. *Pure Appl. Geophys.* **176**, 4069–4109 (2019).
19. F. Amlani et al., Supershear tsunamis: Insights from the M_W 7.5 Palu earthquake. arXiv [Preprint] (2019). https://arxiv.org/abs/1910.14547 (Accessed 27 October 2020).
20. V. V. Titov, C. E. Synolakis, Numerical modeling of tidal wave runup. *J. Waterw. Port, Coast. Ocean Eng.* **124**, 157–171 (1998).
21. T. M. Niemi, N. T. Hall, Historical changes in the tidal marsh of Tomales Bay and Olema Creek, Marin County, California. *J. Coast Res.* **12**, 90–102 (1996).
22. N. Lyberis, Tectonic evolution of the Gulf of Suez and the Gulf of Aqaba. *Tectonophysics* **153**, 209–220 (1988).
23. S. Özalaybey et al., The 1999 İzmit earthquake sequence in Turkey: Seismological and tectonic aspects. *Bull. Seismol. Soc. Am.* **92**, 376–386 (2002).

10 of 11 | PNAS
https://doi.org/10.1073/pnas.2025632118

Elbanna et al.
Anatomy of strike-slip fault tsunami genesis

24. J. Lauterjung, U. Münch, A. Rudloff, The challenge of installing a tsunami early warning system in the vicinity of the Sunda Arc, Indonesia. *Nat. Hazards Earth Syst. Sci.* **10**, 641–646 (2010).
25. P. L. F. Liu, X. Wang, A. J. Salisbury, Tsunami hazard and early warning system in South China Sea. *J. Asian Earth Sci.* **36**, 2–12 (2009).
26. C. E. Gregg *et al.*, Tsunami warnings: Understanding in Hawai'i. *Nat. Hazards* **40**, 71–87 (2007).
27. C. E. Synolakis, E. N. Bernard, Tsunami science before and beyond Boxing Day 2004. *Phil. Trans. Math. Phys. Eng. Sci.* **364**, 2231–2265 (2006).
28. J. Mansinha, D. E. Smylie, The displacement fields of inclined faults. *Bull. Seismol. Soc. Am.* **61**, 1433–1440 (1971).
29. Y. Okada, Internal deformation due to shear and tensile faults in a half-space. *Bull. Seismol. Soc. Am.* **82**, 1018–1040 (1992).
30. Y. Kervella, D. Dutykh, F. Dias, Comparison between three-dimensional linear and nonlinear tsunami generation models. *Theor. Comput. Fluid Dynam.* **21**, 245–269 (2007).
31. J. Wendt, D. D. Oglesby, E. L. Geist, Tsunamis and splay fault dynamics. *Geophys. Res. Lett.* **36**, 1–5 (2009).
32. G. C. Lotto, E. M. Dunham, High-order finite difference modeling of tsunami generation in a compressible ocean from offshore earthquakes. *Comput. Geosci.* **19**, 327–340 (2015).
33. K. J. Ryan, E. L. Geist, M. Barall, D. D. Oglesby, Dynamic models of an earthquake and tsunami offshore Ventura, California. *Geophys. Res. Lett.* **42**, 6599–6606 (2015).
34. A. J. Rosakis, O. Samudrala, D. Coker, Cracks faster than the shear wave speed. *Science* **284**, 1337–1340 (1999).
35. A. J. Rosakis, Intersonic shear cracks and fault ruptures. *Adv. Phys.* **51**, 1189–1257 (2002).
36. E. M. Dunham, R. J. Archuleta, Evidence for a supershear transient during the 2002 Denali Fault earthquake. *Bull. Seismol. Soc. Am.* **94**(6 suppl. B), 256–268 (2004).
37. E. M. Dunham, Conditions governing the occurrence of supershear ruptures under slip-weakening friction. *J. Geophys. Res.* **112**, B07302 (2007).
38. E. M. Dunham, H. S. Bhat, Attenuation of radiated ground motion and stresses from three-dimensional supershear ruptures. *J. Geophys. Res.: Solid Earth* **113**, 1–17 (2008).
39. M. Mello, H. S. Bhat, A. J. Rosakis, H. Kanamori, Reproducing the supershear portion of the 2002 Denali earthquake rupture in laboratory. *Earth Planet Sci. Lett.* **387**, 89–96 (2014).
40. X. Ma, A. E. Elbanna, Effect of off-fault low-velocity elastic inclusions on supershear rupture dynamics. *Geophys. J. Int.* **203**, 664–677 (2015).
41. L. B. Freund, The mechanics of dynamic shear crack propagation. *J. Geophys. Res.: Solid Earth* **84**, 2199–2209 (1979).
42. D. J. Andrews, Rupture velocity of plane strain shear cracks. *J. Geophys. Res.* **81**, 5679–5687 (1976).
43. R. J. Archuleta, Faulting model for the 1979 Imperial Valley earthquake. *J. Geophys. Res.* **89**, 4559–4585 (1984).
44. M. Mello, H. S. Bhat, A. J. Rosakis, Spatiotemporal properties of Sub-Rayleigh and supershear rupture velocity fields: Theory and experiments. *J. Mech. Phys. Solid.* **93**, 153–181 (2016).
45. A. J. Rosakis, V. Rubino, N. Lapusta, Recent milestones in unraveling the full-field structure of dynamic shear cracks and fault ruptures in real-time: From photoelasticity to ultrahigh-speed digital image correlation. *J. Appl. Mech.* **87**, 1–17 (2020).
46. A. J. Rosakis, K. Xia, G. Lykotrafitis, H. Kanamori. "Dynamic shear rupture in frictional interfaces: Speeds, directionality, and modes" in *Earthquake Seismology* (Treatise on Geophysics, Elsevier, Amsterdam, 2007), vol. 4, pp. 183–213.
47. K. Xia, A. J. Rosakis, H. K. Laboratory, Earthquakes: The sub-Rayleigh-to-Supershear rupture transition. *Science* **303**, 1859–1861 (2004).
48. U. Kânoğlu, C. Synolakis, Initial value problem solution of nonlinear shallow water-wave equations. *Phys. Rev. Lett.* **97**, 148501 (2006).
49. V. V. Titov, C. E. Synolakis, Extreme inundation flows during the Hokkaido-Nansei-Oki tsunami. *Geophys. Res. Lett.* **24**, 1315–1318 (1997).
50. Y. Tanioka, K. Satake, Tsunami generation by horizontal displacement of ocean bottom. *Geophys. Res. Lett.* **23**, 861–864 (1996).
51. D. Dutykh, D. Mitsotakis, L. B. Chubarov, Y. I. Shokin, On the contribution of the horizontal sea-bed displacements into the tsunami generation process. *Ocean Model.* **56**, 43–56 (2012).
52. A. Hooper *et al.*, Importance of horizontal seafloor motion on tsunami height for the 2011 M_w=9.0 Tohoku-Oki earthquake. *Earth Planet Sci. Lett.* **361**, 469–479 (2013).
53. E. L. Geist, T. Parsons, Triggering of tsunamigenic aftershocks from large strike-slip earthquakes: Analysis of the November 2000 New Ireland earthquake sequence. *Geochem. Geophys. Geosyst.* **6**, Q10005 (2005).
54. M. Heidarzadeh, A. Muhari, A. B. Wijanarto, Insights on the source of the 28 September 2018 Sulawesi tsunami, Indonesia based on spectral analyses and numerical simulations. *Pure Appl. Geophys.* **176**, 25–43 (2019).
55. V. Rubino, A. J. Rosakis, N. Lapusta, Spatiotemporal properties of sub-Rayleigh and supershear ruptures inferred from full-field dynamic imaging of laboratory experiments. *J. Geophys. Res. Solid Earth* **125**, 1–25 (2020).
56. H. M. Fritz *et al.*, Field survey of the 28 September 2018 Sulawesi tsunami (abstract). *AGU Fall Meeting Abstracts* vol. 2018, NH22B–04 (2018),
57. G. Masselink, P. Russell, Flow velocities, sediment transport and morphological change in the swash zone of two contrasting beaches. *Mar. Geol.* **227**, 227–240 (2006).
58. J. C. Borrero, M. R. Legg, C. E. Synolakis, Tsunami sources in the Southern California Bight. *Geophys. Res. Lett.* **31**, L13211 (2004).
59. C. E. Synolakis, A. C. Yalciner, J. C. Borrero, G. Plafker, "Modeling of the November 3, 1994 Skagway, Alaska Tsunami" in *Solutions to Coastal Disasters '02*. (American Society of Civil Engineers, Reston, VA, 2002), vol. 40605, pp. 915–927.
60. J. Polet, H. Kanamori, Shallow subduction zone earthquakes and their tsunamigenic potential. *Geophys. J. Int.* **142**, 684–702 (2000).
61. M. Heidarzadeh, A. Kijko, A probabilistic tsunami hazard assessment for the Makran subduction zone at the northwestern Indian Ocean. *Nat. Hazards* **56**, 577–593 (2011).
62. T. Baba, P. R. Cummins, T. Hori, Y. Kaneda, High precision slip distribution of the 1944 Tonankai earthquake inferred from tsunami waveforms: Possible slip on a splay fault. *Tectonophysics* **426**, 119–134 (2006).
63. A. Pinar, N. Türkelli, Source inversion of the 1993 and 1995 Gulf of Aqaba earthquakes. *Tectonophysics* **283**, 279–288 (1997).
64. P. Martin Mai, Supershear tsunami disaster. *Nat. Geosci.* **12**, 150–151 (2019).
65. M. Barjous, S. Mikbel, Tectonic evolution of the Gulf of Aqaba-Dead Sea transform fault system. *Tectonophysics* **180**, 49–59 (1990).
66. E. Frucht *et al.*, A fresh view of the tsunami generated by the Dead Sea Transform, 1995 M_w 7.2 Nuweiba earthquake, along the Gulf of Elat–Aqaba. *Seismol Res. Lett.* **90**, 1483–1493 (2019).
67. M. Bouchon *et al.*, How fast is rupture during an earthquake? New insights from the 1999 Turkey earthquakes. *Geophys. Res. Lett.* **28**, 2723–2726 (2001).
68. S. G. Song, G. C. Beroza, P. Segall, A unified source model for the 1906 San Francisco earthquake. *Bull. Seismol. Soc. Am.* **98**, 823–831 (2008).
69. B. Aagaard, C. Williams, M. Knepley. Geodynamics/pylith: PyLith v2.2.1. (2017) https://doi.org/10.5281/zenodo.886600#.X6i0HBJi2P0.mendeley. Accessed 1 August 2019.
70. C. J. Permann *et al.*, {MOOSE}: Enabling massively parallel multiphysics simulation. *SoftwareX* **11**, 100430 (2020).
71. M. Derakhti, R. A. Dalrymple, E. A. Okal, C. E. Synolakis, Temporal and topographic source effects on tsunami generation. *J. Geophys. Res. Oceans* **124**, 5270–5288 (2019).
72. J. L. Hammack, A note on tsunamis: Their generation and propagation in an ocean of uniform depth. *J. Fluid Mech.* **60**, 769–799 (1973).
73. T. S. Stefanakis, F. Dias, C. Synolakis, Tsunami generation above a sill. *Pure Appl. Geophys.* **172**, 985–1002 (2015).

EARTH, ATMOSPHERIC,
AND PLANETARY SCIENCES

Elbanna et al.
Anatomy of strike-slip fault tsunami genesis

PNAS | 11 of 11
https://doi.org/10.1073/pnas.2025632118